



# An innovative constitutive material model for predicting high temperature flow behaviour of inconel 625 alloy

Paul M. Souza<sup>1</sup>, Giribaskar Sivaswamy<sup>1\*</sup> , Luke Bradley<sup>2</sup>, Andrew Barrow<sup>2</sup>, and Salaheddin Rahimi<sup>1</sup>

<sup>1</sup>Advanced Forming Research Centre (AFRC), University of Strathclyde, 85 Inchinnan Drive, Renfrew PA4 9LJ, UK

<sup>2</sup>Rolls-Royce Plc., SW1-70, Raynesway, PO Box 2000, Derby DE21 7XX, UK

**Received:** 17 August 2022

**Accepted:** 29 October 2022

**Published online:**

10 November 2022

© The Author(s) 2022

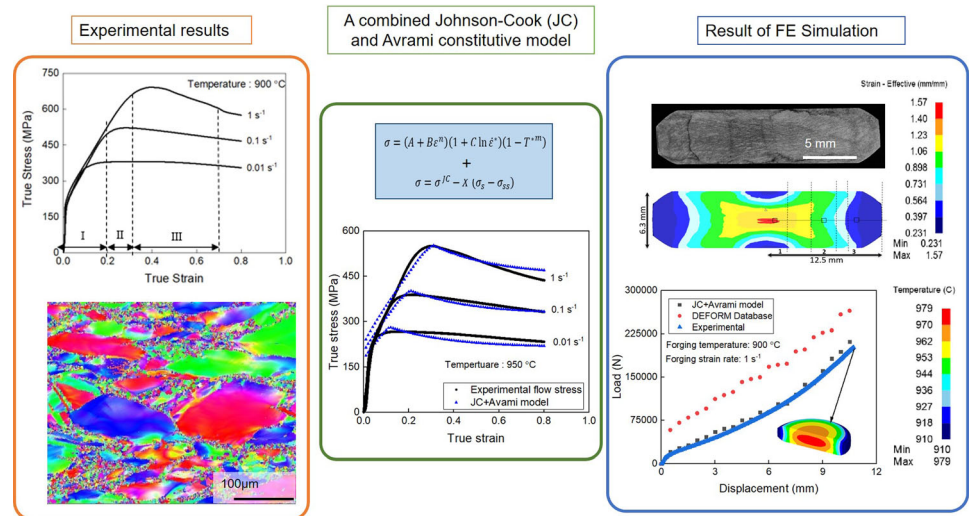
## ABSTRACT

Inconel 625 nickel alloy with its attractive high-temperature strength, excellent corrosion and oxidation resistance is mainly used for critical applications in demanding environments, in both as-cast and wrought conditions. Hot processing of this alloy is crucial for achieving its tailored mechanical properties due to the significant variation in microstructural changes with varying process parameters like temperature, strain, and strain rate. In this study, isothermal hot compression tests were carried out at temperatures ranging from 900 to 1100 °C, and under strain rates ranging from 0.01 to 1 s<sup>-1</sup>. The flow curves revealed three stages of deformation, including a substantial work-hardening stage followed by dynamic recovery and flow softening. Microstructural observations showed the occurrence of discontinuous dynamic recrystallisation (DDRX) as the dominant recrystallisation mechanism during the flow softening. Microstructural analysis suggested that the DRX was more sensitive to the test temperature as compared to the strain rate. An innovative material's constitutive model was developed, by combining Johnson–Cook (JC) and Avrami approaches, to predict work-hardening, dynamic recovery, and flow softening stages of deformation. The predicted flow behavior was in a good agreement with the experimentally measured data. The developed material model was integrated into DEFORM® 3D finite element (FE) simulation software as a user subroutine for the prediction of deformation behaviour in a double truncated cone (DTC) sample. Comparison between the experimentally measured data and the results of FE simulation on the DTC sample showed a very good convergence, indicating the suitability of the proposed material's constitutive model for large scale simulations.

Handling Editor: Megumi Kawasaki

Address correspondence to E-mail: giribaskar.sivaswamy@strath.ac.uk

## GRAPHICAL ABSTRACT



## Introduction

The attractive high temperature mechanical properties and corrosion resistance of nickel-based alloys make them to be one of the extensively used materials for engineering applications in aviation, shipbuilding and nuclear industries [1–4]. The industrial grade solid solution strengthened Inconel 625 (IN625) alloy with its high strength, corrosion and oxidation resistance at elevated temperatures (above 650 °C) is suitable for many applications in nuclear power generation plants like control rod and reactor core components [5–7]. In the aviation sector, the IN625 is used for exhaust, fuel lines, heat exchanger casings, and rocket components. The crevice and pitting corrosion resistance of IN625 makes it a candidate material for high saline underwater applications [8, 9]. Components of IN625 alloy are manufactured mainly through casting and forging routes [10]. This involves careful consideration of process parameters for achieving desired microstructures and hence tailored mechanical properties, which typically requires sequential thermo-mechanical processing (i.e., leading to high manufacturing costs) [11]. Regardless of the attractive properties, the workability of this alloy

is significantly poor, and a relatively fewer materials models exist for predicting the alloy's forming characteristics, compared to other well-known materials such as steels and aluminium alloys [12].

The hot forgeability of materials generally depends on microstructure characteristics (e.g., grain size, precipitation, texture, etc.) and process parameters such as strain, strain rate and the deformation temperature [13–15]. The narrow forgeability window of IN625 poses technological challenges for hot working, which affect the final microstructure and hence the mechanical properties [16–18]. Typically, variations in temperature (e.g., due to temperature gradient), strain and strain rate due to non-uniform plastic deformation result in microstructural heterogeneity such as variation in grain size and localised carbide precipitation, and even surface cracks. Many investigations were carried out to explore the effects of process parameters on deformation behaviour in IN625 alloy [19–23]. These studies have mainly reported the dependency of the material's flow behaviour on strain rate and temperature. Jia et al. [21] has reported a transition in the microstructural evolution mechanisms from DDRX to continuous dynamic recrystallisation (CDRX) with an increase in temperature and reduction in strain rate. An increase

in DRX and reduction in texture intensity with an increase in the deformation temperature has also been reported [20]. A study on the mechanical properties of a solution treated and aged IN625 alloy showed a substantial increase in work-hardening (WH) at lower temperatures and under high strain rates when tested at a range of temperatures and strain rates comprising of 920–1040 °C and  $0.001\text{--}1\text{ s}^{-1}$ . It was also observed that under slower strain rates, there was enough time for dynamic recovery (DRV) to occur concurrently with the WH where the latter was more prevalent [24]. The initial stage of plastic deformation during which both WH and DRV are taking place concurrently, where WH is more dominant, is referred to as the WH + DRV stage.

Mahalle et al. [12] developed a constitutive approach using the Khan-Huang-Liang model to predict flow behaviour in IN625 based on experimental data. The model showed a good convergence of the WH + DRV stage towards the experimentally obtained data, from room temperature to 400 °C. Badrishi et al. [25] implemented a separate approach based on Johnson–Cook (JC) model to predict flow behaviour in the same material, from room temperature to 700 °C, which showed a reasonably good convergence towards experimentally measured data collected via isothermal uniaxial tensile tests. Lin et al. [26] reported a unified dislocation density based model for the prediction of flow behaviour in IN625 during hot compression tests at temperatures between 920 and 1040 °C, which was reasonably accurate. Additionally, Lin et al. [27] reported a Zener Hollomon based approach for the prediction of WH and flow softening in IN625, which was able to predict the overall flow curve for a range of temperatures from 920 to 1040 °C. However, variations reported in the yield strength, suggesting a need for an improved material model to predict flow behaviour in IN625 during hot compression.

Further, Chen et al. [28] developed a unified dislocation density based model to predict DRV and flow softening during hot deformation of nickel-based alloys. The model revealed good accuracy in predicting the flow behaviour of aged nickel alloy. A physically based model developed by Lin et al. [29], using coupled grain size and deformation parameters, showed a reasonably accurate predictions. Furthermore, prediction of hot compression behaviours in different grades of titanium alloy was done by

Souza et al. [14, 30, 31] to a reasonable accuracy using an approach combining Estrin, Mecking and Avrami (EM + Avrami) models. Further, the microstructural based EM + Avrami [32] and comparison with Arrhenius based constitutive model [14] reported substantial versatility of the model. Despite of the good predictive capability of the EM + Avrami model for titanium alloys, the model has not been well proven predicting the WH + DRV stages observed in IN 625 alloy and this needs further investigations.

The present study is aimed to understand the hot deformation behaviour in a solution-annealed IN625 alloy during isothermal hot compression testing. Additional analyses were carried out to understand the three stages of flow behaviour exhibited by the IN 625 alloy, with an emphasis on the WH + DRV and the follow-up flow softening stages. In-depth microstructural characterisations were carried out to understand the dominant recrystallisation mechanisms during deformation. Finally, an innovative constitutive approach has been proposed by combining the JC and Avrami models for the prediction of flow behaviour, which has then been validated using experimentally measured data. The proposed constitutive material model was then used as a user subroutine in a FE simulation using DEFROM® 3D to evaluate its suitability for industrial applications.

## Materials and methods

A forged billet of IN625 alloy with nominal chemical compositions of 21.70% (wt) Cr, 8.60% Mo, 3.70% Nb, 3.70% Fe, 0.40% Ti, 0.2% Mn, 0.12% Si, 0.042% C and balanced nickel, was used in this study. The as-received billet was subjected to an initial solution annealing heat treatment at 1100 °C for 6 h followed by air-cooling to room temperature. Cylindrical samples, with 8 mm diameter and 12 mm height, were extracted from the solution-annealed billet using a wire electrical discharge machine (EDM). The samples were then subjected to hot isothermal compression at five different temperatures (i.e., 900 °C, 950 °C, 1000 °C, 1050 °C and 1100 °C) and under three strain rates ( $0.01\text{ s}^{-1}$ ,  $0.1\text{ s}^{-1}$  and  $1\text{ s}^{-1}$ ). The test temperatures and strain rates were identified as appropriate range for forging of IN625 alloy during open die forging based on previous reports [16, 23]. A Zwick/Roell Z250 mechanical testing machine

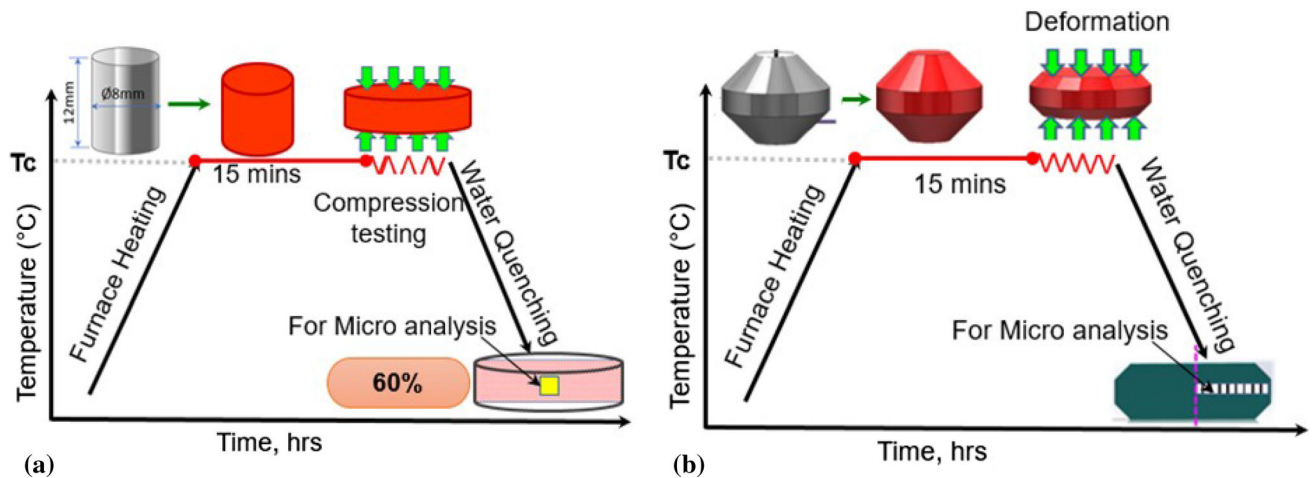


**Figure 1** Schematic representations of the hot compression tests carried out **a** on cylindrical samples and **b** on the DTC samples at different temperatures and strain rates, highlighting the furnace heating, soaking, hot compression and water quenching stages.

fitted with a furnace with three heating zones was used for these tests. The test sample was heated to the target temperature and soaked for 15 min before compression. This is to ensure uniform temperature distribution within the sample. The sample was then subjected to hot compression to  $\sim 60\%$  reduction in height, equivalent to a maximum strain of  $\sim 0.8$  (Fig. 1a). The compressed sample was then water quenched almost immediately (i.e., after  $\sim 4$  s on average) to avoid post deformation microstructural changes. The data obtained from the hot compression tests were corrected for both machine compliance as well as friction and used for further analysis.

For microstructural characterisations, the quenched samples were dissected along the compression axis. The samples were then subjected to standard metallographic sample preparation to a mirror finished condition, followed by 16 h vibratory polishing using  $0.02 \mu\text{m}$  colloidal silica as suspension. The samples were then characterised using an FEI Quanta-650 field-emission gun (FEG) scanning electron microscopy (SEM) interfaced with an Oxford Instrument electron backscattered diffraction (EBSD) camera and an energy dispersive spectroscopy (EDS) detector. Analyses with EDS were carried out to identify carbides potentially formed during and or after the solution annealing treatment. EBSD maps were acquired from the samples at the maximum strain zone (i.e., centre of the cross-section), by applying an accelerating voltage of 20 kV and using a  $100 \mu\text{m}$  dia. aperture. A typical scan area of  $400 \times 300 \mu\text{m}^2$  was mapped for each sample with

$0.3 \mu\text{m}$  step size, where a minimum of 92% of the scanned area was indexed.

### Forgeability analysis

For the validation of the material's model and to understand the forgeability of IN625 alloy, a DTC sample was machined from the solution-annealed billet using EDM, and subjected to isothermal hot compression test at  $900 \text{ }^\circ\text{C}$  under  $1 \text{ s}^{-1}$  nominal strain rate (Fig. 1b). The DTC sample was designed to generate a range of strain magnitudes (i.e.,  $\sim 0.2$ – $1.5$ ) from the centre to the edge of the sample during uniaxial compression. The DTC sample was deformed to  $\sim 60\%$  reduction in height and water quenched immediately after deformation, similarly to the uniaxial compression testing samples, to minimise post deformation microstructural changes (Fig. 1b). The DTC sample was dissected, and the cross-section was metallographically prepared for microstructure characterisations, similarly to the cylindrical samples. The samples were then analysed for grain flow, grain size distribution and dimensional analysis using optical microscopy. The load required to compress the DTC sample up to  $\sim 60\%$  was recorded using a high-speed data logger. The experimentally measured load was compared with the results of FE prediction using the material's model developed in this study, for the purpose of model validation.



## Results

The results of hot compression tests were analysed to understand the effect of process parameters on deformation behaviour and microstructural evolution. The microstructural evolution has been thoroughly investigated. A systematic analysis starting with the initial solution-annealed microstructure to the hot compressed conditions has been carried out using optical microscopy, SEM and EBSD techniques.

## Flow behaviour

A typical flow curve measured for the IN625 alloy consisted of an initial work-hardening stage followed by flow softening beyond a strain level corresponding to the peak stress ( $\varepsilon_p$ ). The flow softening characteristics depend on dominant microstructural deformation mechanisms operating during deformation [33]. The measured true-stress–true-strain curves exhibited work-hardening stage up to the peak stress then switched to a flow softening phase thereafter (Fig. 2). All samples exhibited an increase in the flow stress with lower deformation temperatures and higher strain rates (Fig. 2). The samples

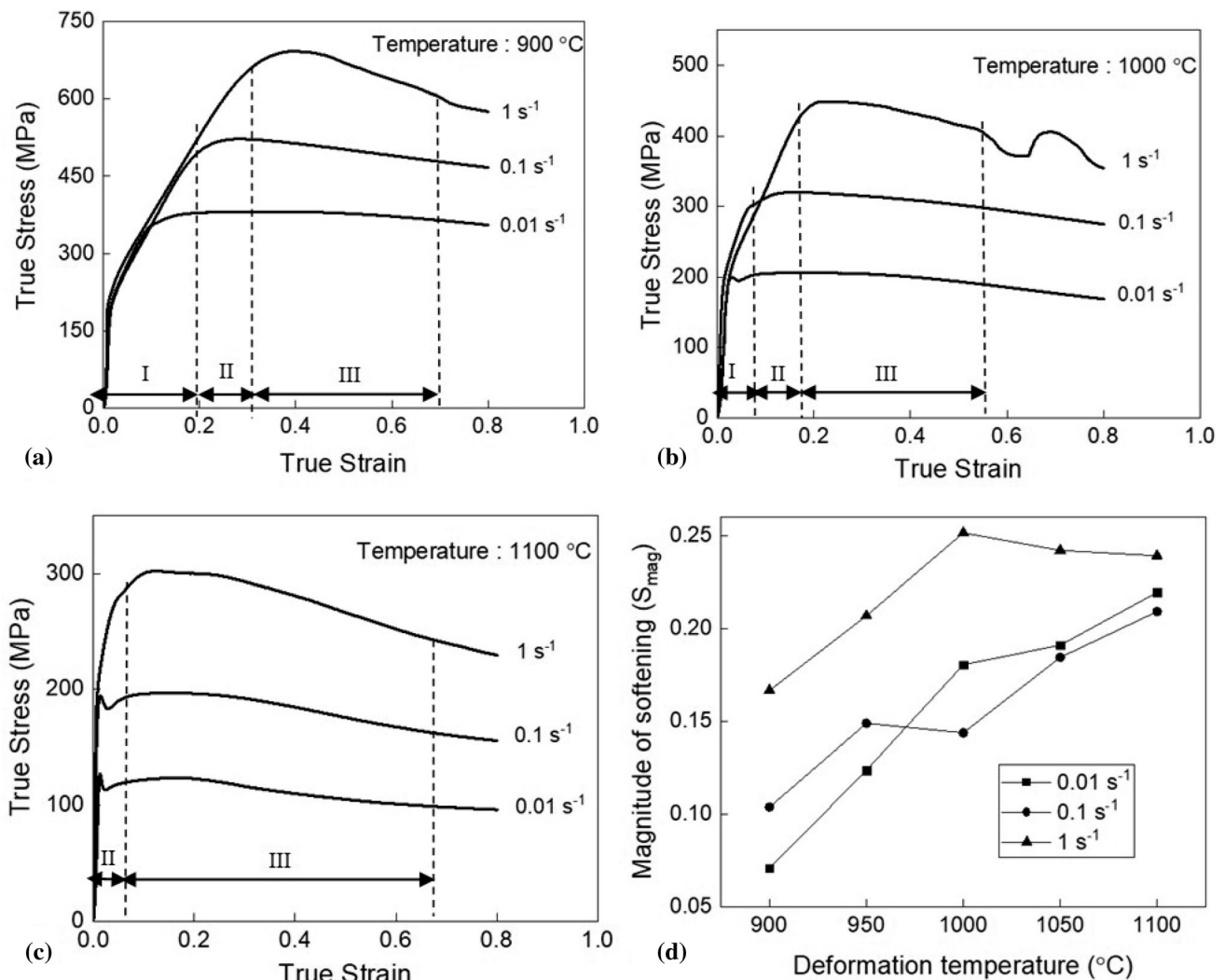


**Figure 2** True-stress versus true-strain curves measured for the IN625 under different strain rates at **a** 900 °C, **b** 1000 °C, and **c** 1100 °C. **d** Plots of the magnitude of flow softening as a function of temperature and strain rate calculated using Eq. (1). Note that

various stages of deformations in the flow curves are highlighted in (a), (b) and (c), where stage I in c is not visible due to its narrow range.

compressed under  $1\text{ s}^{-1}$  showed significant work-hardening, especially those tested at or below  $1000\text{ }^\circ\text{C}$  (Fig. 2a, b). Similar results were reported before for IN625 where the flow curve was divided into three stages of deformation denoted as stage I, stage II and stage III [24]. Similarly, these stages are distinguished in the measured flow curves, as shown in Fig. 2a. In stage I, the material undergoes work-hardening and DRV concurrently where the former is more dominant, followed by stress stabilisation in stage II, and a combination of work-hardening, DRV and DRX in stage III where the latter are more dominant [34]. While these stages can be clearly identified in those tests conducted at or under  $1000\text{ }^\circ\text{C}$ , the increase in temperature to  $1100\text{ }^\circ\text{C}$  led to a relatively shorter work-hardening stage (Fig. 2c). The substantial difference in work-hardening as a function of temperature, has resulted in significant variation in peak stress.

Increase in the strain rate and deformation temperature was observed to result in greater level of flow softening (Fig. 2d). The flow softening was quantified by calculating the flow softening magnitude ( $S_{\text{mag}}$ ) using an approach given by Semiatin et al. [35], shown in Eq. (1).

$$S_{\text{mag}} = \Delta\sigma / \sigma_p \tag{1}$$

where  $\sigma_p$  is the peak stress and  $\Delta\sigma = \sigma_p - \sigma(0.8)$  represents the difference between the peak stress and the stress at 0.8 strain where the maximum softening is achieved. A maximum of  $\sim 25\%$  softening was measured for the samples tested at  $1000\text{ }^\circ\text{C}$  under  $1\text{ s}^{-1}$  strain rate.

### Strain rate sensitivity

The flow curves derived from the hot compression tests showed a significant increase in the measured flow stress with higher strain rates (Fig. 2). This has been further analysed by determining the strain rate sensitivity ( $m$ ) from the measured flow curves. The strain rate sensitivity can be measured using the gradient of stress as a function of strain rate at a given strain and temperature, according to Eq. (2) [36].

$$m = \left. \frac{d \log \sigma}{d \log \dot{\epsilon}} \right|_{\epsilon, T} \tag{2}$$

where  $\sigma$  is the flow stress at a given strain and deformation temperature ( $T$ ),  $\dot{\epsilon}$  is the strain rate, and  $\epsilon$  is the strain. The strain rate sensitivity as a function of

strain for varying deformation temperature suggest an increasing trend with temperature (Fig. 3a). It is apparent that the strain rate sensitivity increases drastically at the beginning of the deformation (i.e., lower strain levels) until it reaches a steady state level for most deformation conditions. This variation in the strain rate sensitivity suggests that different microstructural evolutionary mechanisms are operational under these deformation conditions.

### Strain hardening behaviour

The strain hardening exponent ( $n$ ) is a measure of strain hardening in a material, which is an important parameter for work-hardening during hot deformation. It can be used to understand the dominance of strain hardening compared to flow softening occurring concurrently during deformation [37]. Thus, the  $n$  for the hot compression tests can be evaluated using Eq. (3).

$$n = \left. \frac{d \log \sigma}{d \log \epsilon} \right|_{\dot{\epsilon}, T} \tag{3}$$

where  $\sigma$  is the flow stress and  $\epsilon$  is the strain under constant deformation temperature and strain rate.

The calculated  $n$  values as a function of temperature for the tests carried out under different strain rates, which are in the strain range of 0.03 to 0.55, are shown in Fig. 3b. It is apparent that both the deformation temperature and strain rate affect the  $n$  considerably during the isothermal compression tests. An increase in  $n$  was measured with an increase in strain rate and a decrease in the test temperature (Fig. 3b). Meanwhile, for the test performed under the lowest strain rate (i.e.,  $0.01\text{ s}^{-1}$ ), the observed  $n$  was significantly lower (0.03 to 0.05) except those of the tests conducted at  $900\text{ }^\circ\text{C}$  and  $950\text{ }^\circ\text{C}$ . Such lower hardening exponents were also measured for the tests carried out under  $0.1\text{ s}^{-1}$  strain rate at temperatures above  $1050\text{ }^\circ\text{C}$ . On the other hand, the highest  $n$  was obtained for the tests conducted under the highest strain rate (i.e.,  $1\text{ s}^{-1}$ ), irrespective of the test temperature.

### Activation energy for deformation

The flow stress values obtained from the hot compression tests were used to calculate the activation energy for deformation. According to Zener and Hollomon [38] relationship, the rate of deformation at

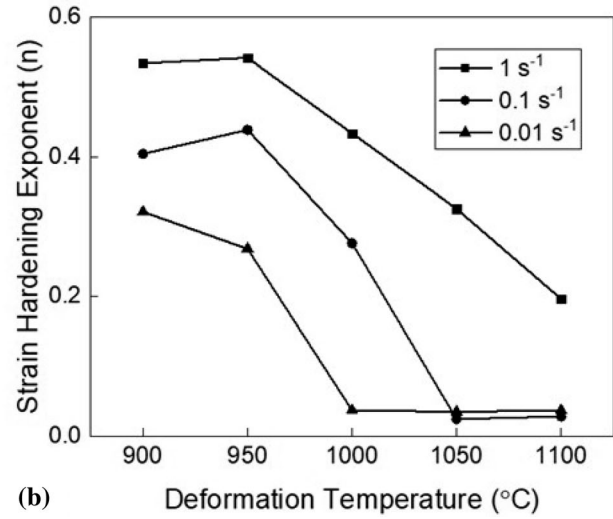
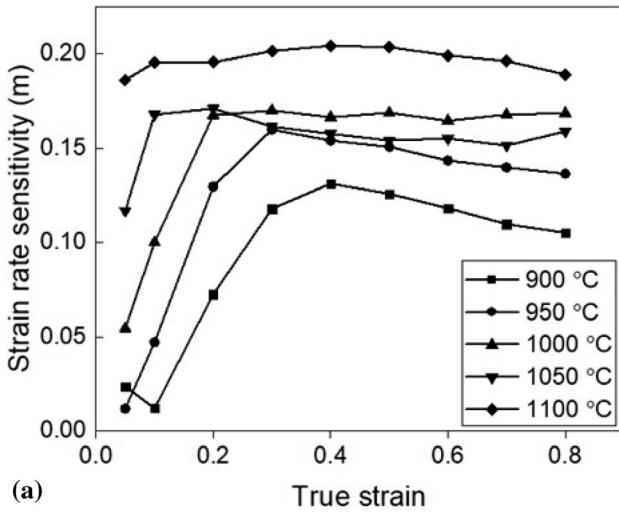


**Figure 3** **a** Strain rate sensitivity as a function of strain at varying temperatures measured using the plots of  $\log(\sigma)$  versus  $\log(\dot{\epsilon})$  during the hot compression tests, and **b** Strain hardening

exponents for varying temperatures and strain rates calculated using the plots of  $\log(\sigma)$  versus  $\log(\dot{\epsilon})$  during the initial work-hardening stage for the IN625 alloy.

high temperature is controlled by the thermal activation energy of the material. Thus, Zener Hollomon parameter ( $Z$ ), which relates strain rate ( $\dot{\epsilon}$ ) and temperature ( $T$ ) is given in Eq. (4), and the strain rate ( $\dot{\epsilon}$ ) is defined in Eq. (5).

$$Z = \dot{\epsilon} \exp\left(\frac{Q}{RT}\right) \tag{4}$$

$$\dot{\epsilon} = AF(\sigma) \exp\left(-\frac{Q}{RT}\right) \tag{5}$$

$$F(\sigma) = \begin{cases} \sigma^{n_1} & \alpha\sigma < 0.8 \\ \exp(\beta\sigma) & \alpha\sigma > 1.2 \\ [\sinh(\alpha\sigma)]^{m_2} & \text{for all } \sigma \end{cases}$$

where  $Q$  is the activation energy for deformation ( $\text{J mol}^{-1}$ ),  $R$  is the universal gas constant ( $8.3145 \text{ J mol}^{-1} \text{ K}^{-1}$ ) and  $A, \alpha, \beta$  and  $n$  are the material constants. Equations (4) and (5) are only applicable for a constant strain. Hence, the activation energy was calculated for the peak stress ( $\sigma_p$ ). The values for  $F(\sigma)$  varies depending upon the stress level such that for the low and high stress levels Eq. (5) takes the following forms.

$$\dot{\epsilon} = B\sigma^{n_1} \tag{6}$$

$$\dot{\epsilon} = C \exp(\beta\sigma) \tag{7}$$

where  $B$  and  $C$  are material constants. Taking both equations into logarithmic scales lead to Eqs. (8) and (9), respectively.

$$\ln(\sigma) = \frac{1}{n_1} \ln(\dot{\epsilon}) - \frac{1}{n_1} \ln(B) \tag{8}$$

$$\sigma = \frac{1}{\beta} \ln(\dot{\epsilon}) - \frac{1}{\beta} \ln(C) \tag{9}$$

Thus, from Eq. (8), the material constant  $n_1$  can be obtained as the inverse slope of the  $\ln(\sigma_p)$  versus  $\ln(\dot{\epsilon})$ , as shown in Fig. 4a. The average of the inverse slopes at all peak stresses was calculated to be  $6.02 \text{ MPa}^{-1}$ , which is considered as  $n_1$  for the IN625 alloy investigated in this work. Similarly, the material constant  $\beta$  was also obtained from Eq. (9) as the inverse slope of  $\sigma_p$  versus  $\ln(\dot{\epsilon})$  curve, as shown in Fig. 4b, and the average was calculated to be  $0.019 \text{ MPa}^{-1}$ . Thus,  $\alpha = \beta/n_1$  was calculated as  $0.0032 \text{ MPa}^{-1}$ .

Furthermore, for all stress levels substituting  $F(\sigma)$  in Eq. (5) leads to Eq. (10), which takes the form of Eq. (11) in logarithmic scale.

$$\dot{\epsilon} = A[\sinh(\alpha\sigma)]^{m_2} \exp\left(-\frac{Q}{RT}\right) \tag{10}$$

$$\ln[\sinh(\alpha\sigma)] = \frac{\ln(\dot{\epsilon})}{n_2} + \frac{Q}{nRT} - \frac{\ln A}{n_2} \tag{11}$$

Thus, for a given deformation temperature and strain rate, integrating Eq. (11) leads to Eqs. (12) and (13).

$$\frac{1}{n_2} = \frac{d\{\ln[\sinh(\alpha\sigma)]\}}{d\{\ln(\dot{\epsilon})\}} \tag{12}$$

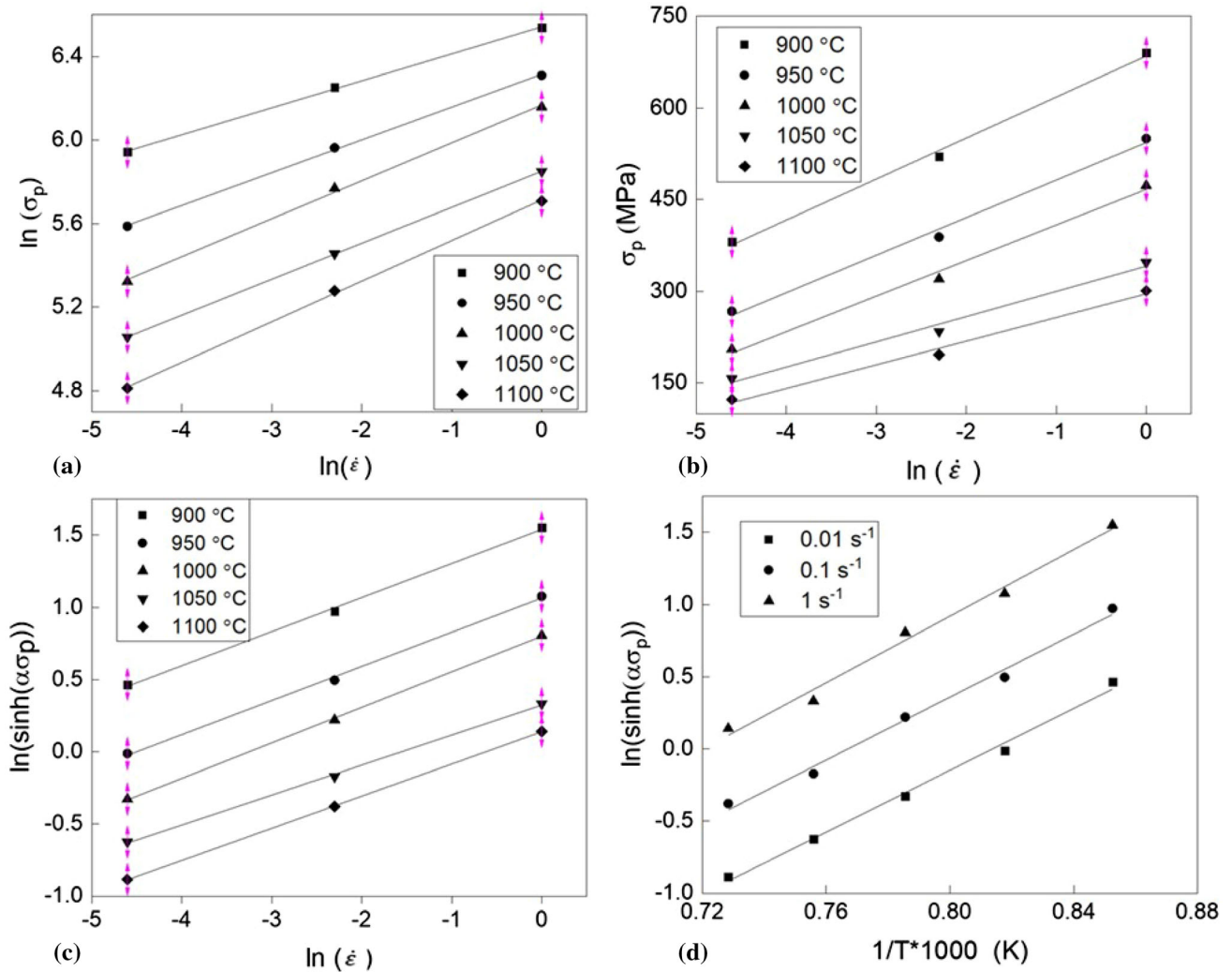


**Figure 4** **a** Plots of  $\log(\sigma_p)$  versus  $\log(\dot{\epsilon})$  for varying temperatures, **b** plots of  $\sigma_p$  versus  $\log(\dot{\epsilon})$  for varying temperatures, for the evaluation of  $\beta$  and  $n_1$ , respectively from Eq. (8) and (9), **c** plots of  $\log(\sinh(\alpha\sigma_p))$  versus  $\log(\dot{\epsilon})$  for varying

temperatures for the evaluation of  $n_2$ , and **d** plots of  $\log(\sinh(\alpha\sigma_p))$  versus  $\frac{1}{T} * 1000$  for varying temperatures, used for the evaluation of parameters in Eqs. (12) and (13), respectively.

$$Q = n_2 R \frac{d\{\ln[\sinh(\alpha\sigma)]\}}{d(1/T)} \tag{13}$$

The value of  $n_2$  was then calculated to be 4.25 MPa as the inverse slope of  $\ln[\sinh(\alpha\sigma)]$  versus  $\ln(\dot{\epsilon})$  curve (Fig. 4c). The average activation energy for deformation at peak stress under different strain rates was also calculated from Eq. (13) as 381 kJ mol<sup>-1</sup> (Fig. 4d). Similar values for activation energy were reported for IN625 alloy (i.e., ~ 394 kJ mol<sup>-1</sup>) for a range of temperatures and strain rates, similar to those implemented in this study, suggesting the occurrence of significant dynamic recrystallisation [20].

### Microstructural analyses

#### Microstructural characteristics after solution annealing

Microstructural analysis of the as solution-annealed followed by air cooled condition revealed equiaxed  $\gamma$  grains with varying grain size, with presence of a significant number of annealing twins (Fig. 5a, b). Carbide particles, precipitated within  $\gamma$  grains and along the grain boundaries, were also observed (Fig. 5c). Typically, prolonged heat treatments (i.e., in excess of 0.5 h) at temperatures ranging from 800 °C to 1050 °C leads to the formation of M<sub>23</sub>C<sub>6</sub> and M<sub>6</sub>C type carbides in IN625 [39, 40]. The results of Energy



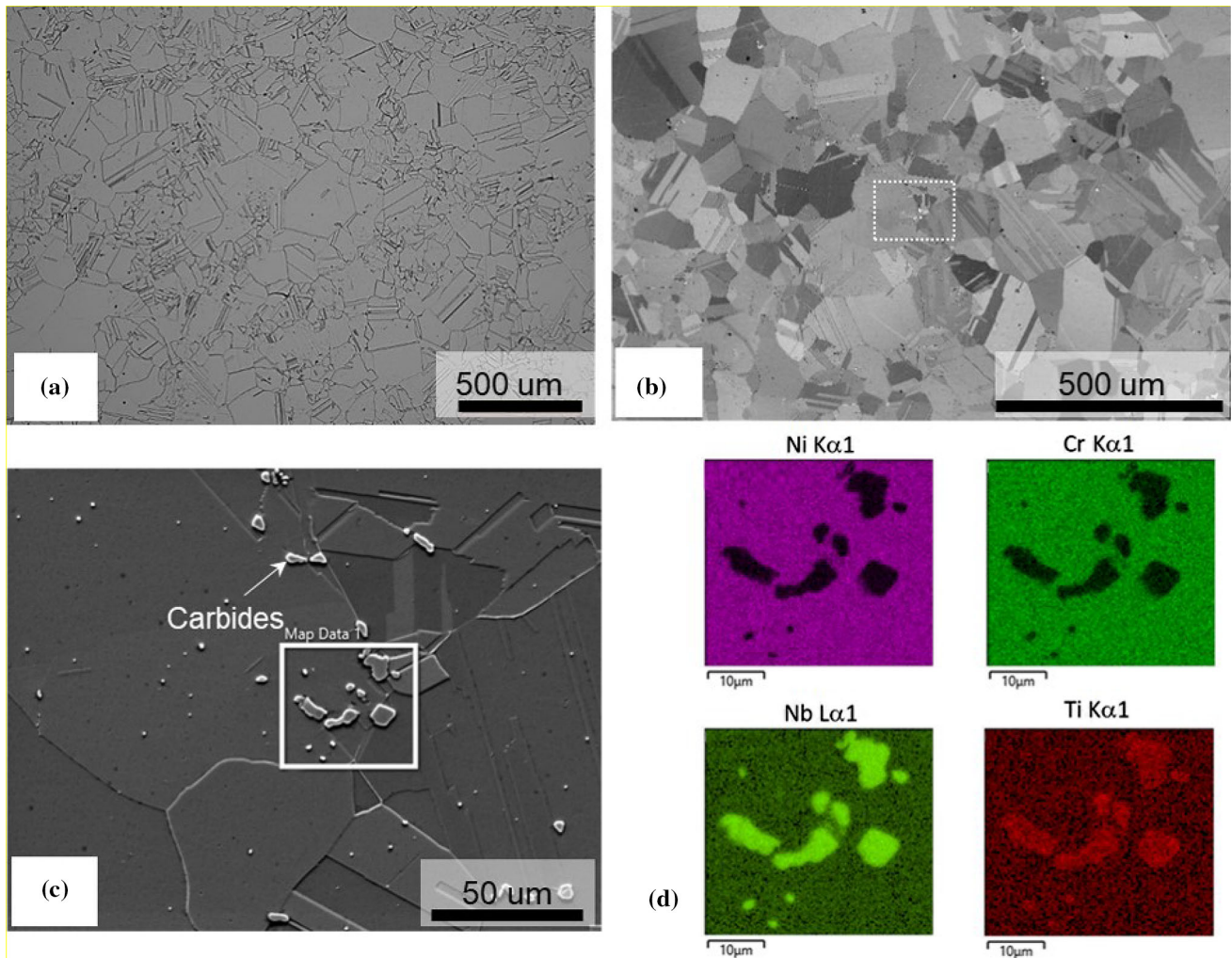


**Figure 5** Microstructural characteristics of the IN625 alloy in the solution-annealed (6 h at 1100 °C) followed by air-cooled condition **a** Optical micrograph recorded at lower magnification showing the equi-axed  $\gamma$  grains with and with-out twins **b** A backscattered SEM micrograph showing carbides distribution in  $\gamma$

matrix with grains of varying sizes and the presence of annealing twins, **c** Higher magnification micrograph from the region marked by dotted rectangle showing the large blocky (Nb, Ti)C carbides and the rectangular area used for EDS analysis. **d** EDS maps showing the presence of Nb and Ti rich carbides.

dispersive spectroscopy (EDS) analysis show the presence of large blocky niobium and titanium based carbides (Nb, Ti)C. Similar niobium and titanium rich carbides are also reported in literature [40]. The solution annealed IN625 material had a heterogeneous microstructure with a relatively broad grain size distribution varying from few microns to a maximum of 45  $\mu\text{m}$ .

#### *Microstructural characteristics after hot compression tests*

The microstructural analyses on the samples deformed to 0.8 true strain at 900 °C under different strain rates, demonstrate variations in the fraction of

grains underwent DRX as a function of strain rate (Fig. 6a–c). The EBSD inverse pole figure (IPF) maps, with respect to the compression direction revealed that the grain boundaries of the parent  $\gamma$  grains decorated by strain free recrystallised grains formed during hot compression tests. The formation of necklace structure along the pre-existing grain boundaries is a characteristic of DDRX occurred during the deformation [41]. The extent of fine grain formation along the parent grain boundaries (i.e., through DDRX) depends on the initial grain size, the deformation temperature and strain rate [42]. It can be observed from the EBSD IPF maps that the increase in strain rate has major effect on the number



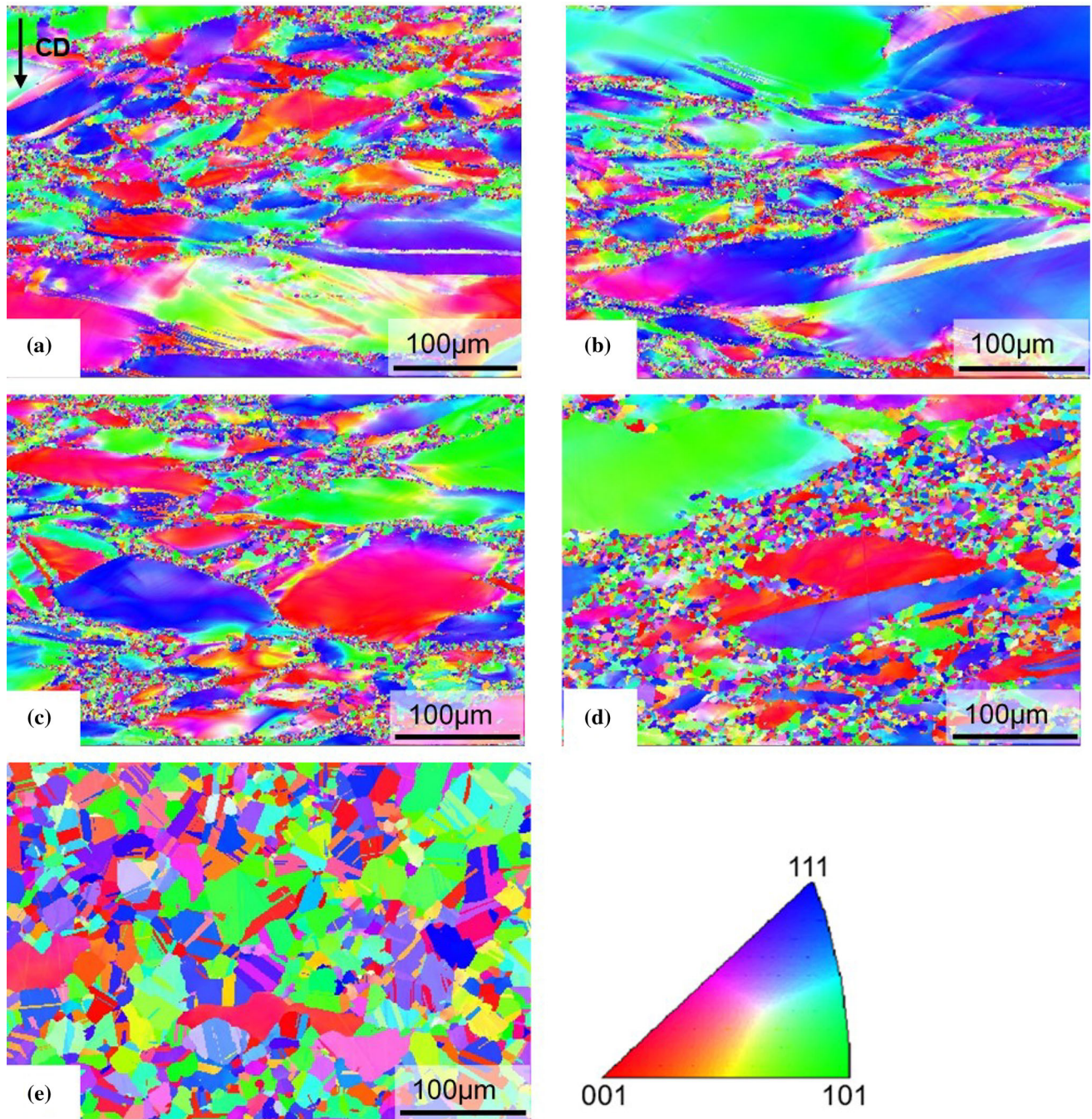


**Figure 6** EBSD IPF colouring maps with respect to the compression direction (CD), showing the variations in grain structure after deformation to 0.8 true strain at varying

temperatures and strain rates, **a** 900 °C and 0.01 s<sup>-1</sup>, **b** 900 °C and 0.1 s<sup>-1</sup>, **c** 900 °C and 1 s<sup>-1</sup>, **d** 1000 °C and 0.01 s<sup>-1</sup> and **e** 1100 and 0.01 s<sup>-1</sup>.

of grain boundaries with fine grains and on the fraction of the necklace structures formed (Fig. 6a–c). It is also clear from these maps that there is an inhomogeneity in DDRX, as the grain boundaries of some pre-existing  $\gamma$  grains have no evidence of fine

grain formation, irrespective of the applied strain rate (Fig. 6a–c).

The post-deformation microstructures of the samples tested under 0.01 s<sup>-1</sup> strain rate at higher temperatures (i.e., 1000 °C and 1100 °C) show a substantial difference in the fraction and size of the

grains underwent DRX (Fig. 6d, e). From the characteristic necklace structure, it is apparent that at 900 °C DRX was initiated, although the temperature was not sufficiently high for a significant progress in recrystallisation and grain growth (Fig. 6a), whereas by increasing the temperature to 1000 °C, the fraction of grains underwent DRX was drastically increased with significant grain growth (Fig. 6d). Further increase in temperature under the same strain rate (i.e.,  $0.01 \text{ s}^{-1}$ ) has resulted in not only complete recrystallisation, but also a substantial grain growth (Fig. 6e).

The fraction of recrystallised grains in these microstructures were assessed using HKL Channel 5 software to understand the effect of strain rate and temperature on the onset of recrystallisation (Fig. 7). For these analyses, grains with misorientation less than  $2^\circ$  were considered as recrystallised,  $2^\circ$  to  $7.5^\circ$  as sub-structured and those above  $7.5^\circ$  as deformed. Although a negligible difference (i.e., less than 2%) was seen for the samples tested at 900 °C under smaller strain rates of  $0.01 \text{ s}^{-1}$  and  $0.1 \text{ s}^{-1}$  (Fig. 6a, b), a fairly high increase in the fraction of recrystallised grains (i.e., 28%) was observed for the test carried out at the same temperature under the higher strain rate ( $1 \text{ s}^{-1}$ ) (i.e., Figs. 6c, 7a). On the other hand, the observed and measured substantial increase in the fraction of recrystallised grains (Fig. 7b) with an increase in the deformation temperature supports the measured softening behaviours presented in Fig. 2d. The increase in strain rate to  $1 \text{ s}^{-1}$  and/or increasing deformation temperature to 1100 °C has led to the

increase in fraction of dynamically recrystallised grains as compared to lower strain rates and temperatures, which is clearly observed in the histogram in Fig. 7a, b. These suggest that the driving force for dynamic recrystallisation is higher at higher temperatures, which leads to the formation of recrystallised grains. Therefore, the lower measured volume fraction for the deformed grains within the investigated area by EBSD is due to higher fraction of recrystallised grains (i.e., more deformed grains converted to recrystallised grains).

## Discussion

The measured flow curves exhibited three stages of deformation, including an initial elastic region, leading to a substantial work-hardening stage, followed by a final flow softening. The work-hardening behaviour of the alloy has often been linked with the rate of work-hardening [43]. The temperature and the applied strain rate determine the dislocation density evolution and the work-hardening rate. At lower temperatures the diffusion rate of vacancies is reduced and dislocation density is increased, which in turn lead to higher level of work-hardening with increased interaction with the carbides and precipitates [24]. The increased dislocation density at higher strain rates further delays the dynamic recovery at hot deformation temperatures leading to a combined WH + DRV stage [19]. On the other hand, the measured flow softening occurred beyond the peak stress

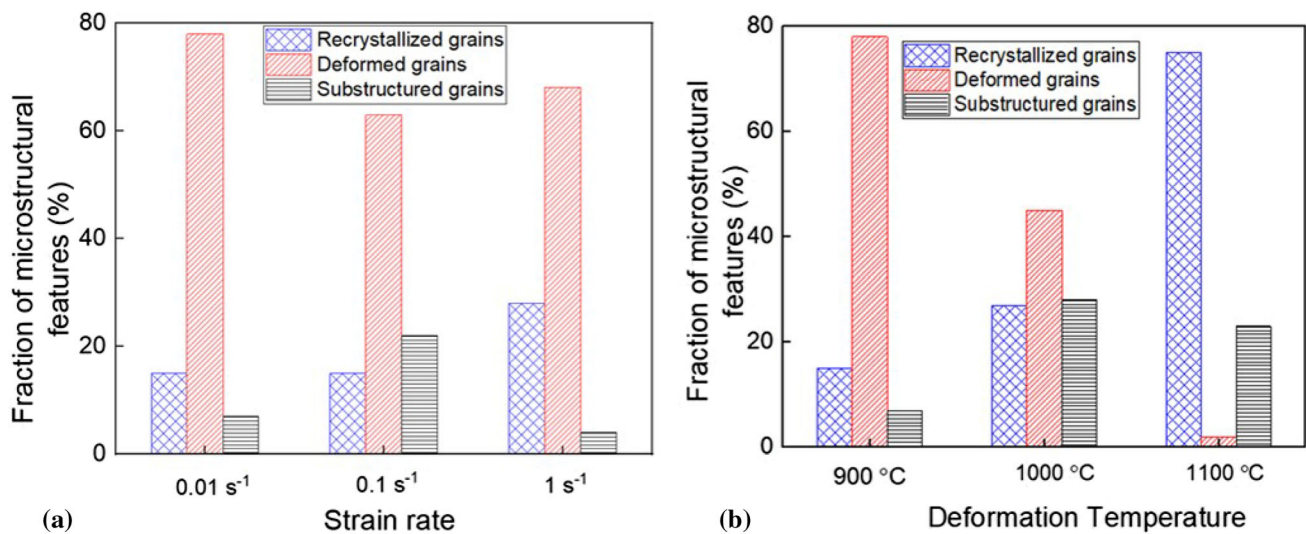


**Figure 7** Histograms showing the fractions of recrystallised, sub-structured and deformed grains for the microstructures in Fig. 6.



for different strain rates were mainly related to the initiation of onset of DRX, which is also a function of deformation temperature and strain rate (Figs. 6, 7) [18]. The initiation of flow softening was delayed for the test conducted at a lower temperature and under the higher strain rate conditions. Whereas, at higher temperatures and under lower strain rates the flow softening accelerated, implying the dependency of the kinetics of DRX on temperature and strain rate (Fig. 2a, b). This is evident in the EBSD IPF maps shown in Fig. 6 whereby higher fractions of recrystallised grains were measured for the latter. The increase in temperature beyond the precipitate's solvus temperature (i.e., above 1000 °C) has led to significant levels of recrystallisation and grain growth (Fig. 6e). These observations suggest that for the IN625 investigated in this study, DRX is more sensitive to the test temperature than the strain rate.

The DRX mechanism has typically been classified into continuous, discontinuous and geometric [44]. The formation of fine strain free grains as result of fragmentation of the initial grains due to the conversion of low angle boundaries to high angle boundaries is known as CDRX [45]. Whereas, the nucleation of fine strain free grains as a result of strain induced bulging and fragmentation at the boundaries of the parent grains is referred to as DDRX [46]. The formation of necklace structure (i.e., fine recrystallised grains along the grain boundaries) at lower temperatures is due to strain localisation beyond a threshold required for DRX at grain boundaries [16, 17]. Alternatively, severe plastic deformation (SPD) processes such as equal channel angular pressing (ECAP), accumulative roll bonding (ARB) and high pressure torsion tests (HPT) results in coalescence of the existing high angle boundaries leading to the formation of fine strain free grains which is termed as geometric dynamic recrystallisation (GDRX) [47]. The IN625 alloy studied in this work revealed the necklace structure around the parent grains for all test conditions, with variation in size and distribution of recrystallised grains and their fractions depending on the applied process parameters (i.e., temperature and strain rate). This suggest that the DDRX is the dominant deformation mechanism for IN625 with the present processing and microstructural conditions.

The driving force for dynamic recovery followed by recrystallisation is expected to be high at higher deformation temperatures. This is due to the

increased dislocation annihilation mechanisms leading to reduced dislocation density and nucleation of strain free grains within and/or along the grain boundaries of parent grains [18]. The recovery mechanisms such as dislocation climb, dislocation cross slip, and dislocation annihilation (polygonisation) are also expected to be high at higher testing temperatures. In addition, the formation of twins at high temperatures can substantially decrease the dislocation density [48].

## Constitutive modelling of flow behaviour

### JC approach for the prediction of work-hardening

The measured flow curves exhibited an initial work-hardening and DRV stage, which occurs concurrently with the former being dominant, followed by flow softening beyond the peak stress (Fig. 2). The extent of the initial stage was mainly dependant on the process parameters, whereas the flow softening stage was similar for all conditions. In this study, it has been attempted to predict the measured flow behaviour by combining JC model for the initial stage of work-hardening and DRV, and Avrami model for the flow softening stage.

The widely used JC constitutive material model has been shown to effectively predict the flow stress as a function of strain, strain rate and temperature [49]. The JC model is a simplified approach with readily available constants for various materials due to its isotropic nature. This model describes the flow stress ( $\sigma$ ) as a function of plastic strain ( $\epsilon$ ), strain rate ( $\dot{\epsilon}$ ) and absolute temperature ( $T$ ), according to Eq. (14) [50].

$$\sigma = (A + B\epsilon^n)(1 + C \ln \dot{\epsilon}^*) (1 - T^{*m}) \quad (14)$$

where  $A$  is the yield stress at the reference  $\dot{\epsilon}$  and  $T$ , which is 204 MPa,  $B$  is the strain hardening coefficient,  $n$  is the strain hardening exponent and  $C$  and  $m$  are the strain rate strengthening coefficient and thermal softening coefficient, respectively.

The dimensionless strain rate ( $\dot{\epsilon}^*$ ) is measured by dividing the actual  $\dot{\epsilon}$  to a reference  $\dot{\epsilon}_0 = 0.001 \text{ s}^{-1}$  considered for the present study. The homologous temperature ( $T^*$ ) is calculated as a function of absolute temperature, reference temperature ( $T_r = 800^\circ\text{C} \leq T$ ) and the melting temperature ( $T_m = 1335^\circ\text{C}$  [51]).

$$\dot{\varepsilon}^* = \frac{\dot{\varepsilon}}{\dot{\varepsilon}_0} \quad (15)$$

$$T^* = \frac{T - T_r}{T_m - T_r} \quad (16)$$

To calculate the constants  $B$  and  $n$ , the absolute temperature and strain rate were considered at the reference state such that Eq. (14) was re-written as Eq. (17), and by taking it to logarithmic scale as Eq. (18).

$$\sigma = (A + B\varepsilon^n) \quad (17)$$

$$\ln(\sigma - A) = \ln B + n \ln \varepsilon \quad (18)$$

The  $n$  and  $B$  values were calculated as the slope and intercept of the  $\ln(\sigma - A)$  versus  $\ln \varepsilon$  curve with the vertical axis. An average of 0.8945 MPa for  $n$  and 898 MPa for  $B$  were calculated. To determine the material constant  $C$ , an absolute reference temperature ( $T_r = 800^\circ\text{C}$ ) was considered. Hence, Eq. (14) was resulted in Eq. (19).

$$\sigma = (A + B\varepsilon^n)(1 + C \ln \dot{\varepsilon}^*) \quad (19)$$

By rearranging Eq. (19), the strain rate strengthening coefficient  $C$  can be obtained from the slope of  $\frac{\sigma}{(A+B\varepsilon^n)}$  versus  $\ln \dot{\varepsilon}^*$  curve. For this, stress values for varying strain from 0.05 to 0.2 with an interval of 0.025 was considered for varying strain rates. A slope of 0.07252 was calculated for  $C$ , using the concentrated linear fit for all the strain values.

Further, to determine the thermal softening coefficient ( $s$ ) at the reference strain rate, Eq. (14) was re-written as Eq. (20) by considering the function  $(1 + C \ln \dot{\varepsilon}^*)$  equal to unity.

$$\sigma = (A + B\varepsilon^n)(1 - T^{*s}) \quad (20)$$

The constant  $s$  was then obtained from the slope of  $\ln\left(1 - \frac{\sigma}{(A+B\varepsilon^n)}\right)$  versus  $\ln(T^*)$  curve. Stress values for the strain range (0.05 to 0.2) were taken for varying temperatures. A slope of 1.051 was measured for the constant  $s$  using the concentrated linear fit for all the strain values.

The results predicted by the JC model for the initial work-hardening stage was converging well (i.e., 97% accuracy) towards the experimentally measured data for varying temperatures and strain rates conditions (Fig. 8a), considering the evaluated constants and coefficients explained earlier. Hence, the JC model can be used to predict the flow behaviour at initial

stage of deformation with a reasonable accuracy, for the explored temperature and strain rate ranges in this study.

### Combined Avrami and JC model for the prediction of flow softening

The JC empirical approach was not suitable for the prediction of the flow behaviour during the flow softening (i.e., beyond a strain corresponding to the peak stress ( $\varepsilon_p$ )). Therefore, Avrami approach was considered for the flow softening stage of the flow curve [30, 31]. The conventional Avrami equation was combined with Eq. (14), which is denoted as the JC + Avrami model hereafter (Eq. 21).

$$\sigma = \sigma^{JC} - X(\sigma_s - \sigma_{ss}) \quad \text{for } \varepsilon > \varepsilon_p \quad (21)$$

In Eq. (21), the flow stress predicted by the JC approach was normalised by the saturation stress ( $\sigma_s$ ), termed as  $\sigma^{JC}$ ,  $X$  is the fraction of microstructure underwent DRX at a specific strain ( $0 < X \leq 1$ ), and  $\sigma_{ss}$  is the steady state stress (i.e., at 0.8 strain). The fraction of recrystallisation at any strain beyond  $\varepsilon_p$  can be expressed as,

$$X = \frac{\sigma^{JC} - \sigma}{\sigma_s - \sigma_{ss}} = 1 - \exp\left(-a(\varepsilon - \varepsilon_p)^b\right) \quad (22)$$

and

$$\ln\left(\ln\frac{1}{(1-X)}\right) = \ln a + b \ln(\varepsilon - \varepsilon_p) \quad (23)$$

The constants  $a$  and  $b$  were respectively determined from the slope of the  $\ln\left(\ln\frac{1}{(1-X)}\right)$  versus  $\ln(\varepsilon - \varepsilon_p)$  curve and its intercept with the vertical axis for  $\varepsilon > \varepsilon_p$ . Minor variations observed in the material constants for different temperatures and strain rates were omitted to reduce the complexity of the model. The material constants  $a$  and  $b$  were calculated as 1.1 and 4.2 respectively and considered to be uniform for all strain rates and temperatures. The uncertainties in predicting the fraction of recrystallisation and flow softening were reduced by considering average values for  $a$  and  $b$ . Further, the number of variables were reduced by calculating  $\sigma_s$ ,  $\sigma_{ss}$  and  $\varepsilon_p$  as functions of Zener-Hollomon parameter ( $Z$ ). A 2nd order polynomial fit was considered as the best fit and therefore used to calculate  $\sigma_s$ ,  $\sigma_{ss}$  and  $\varepsilon_p$  as a function of  $\log(Z)$  (Fig. 8b–d).



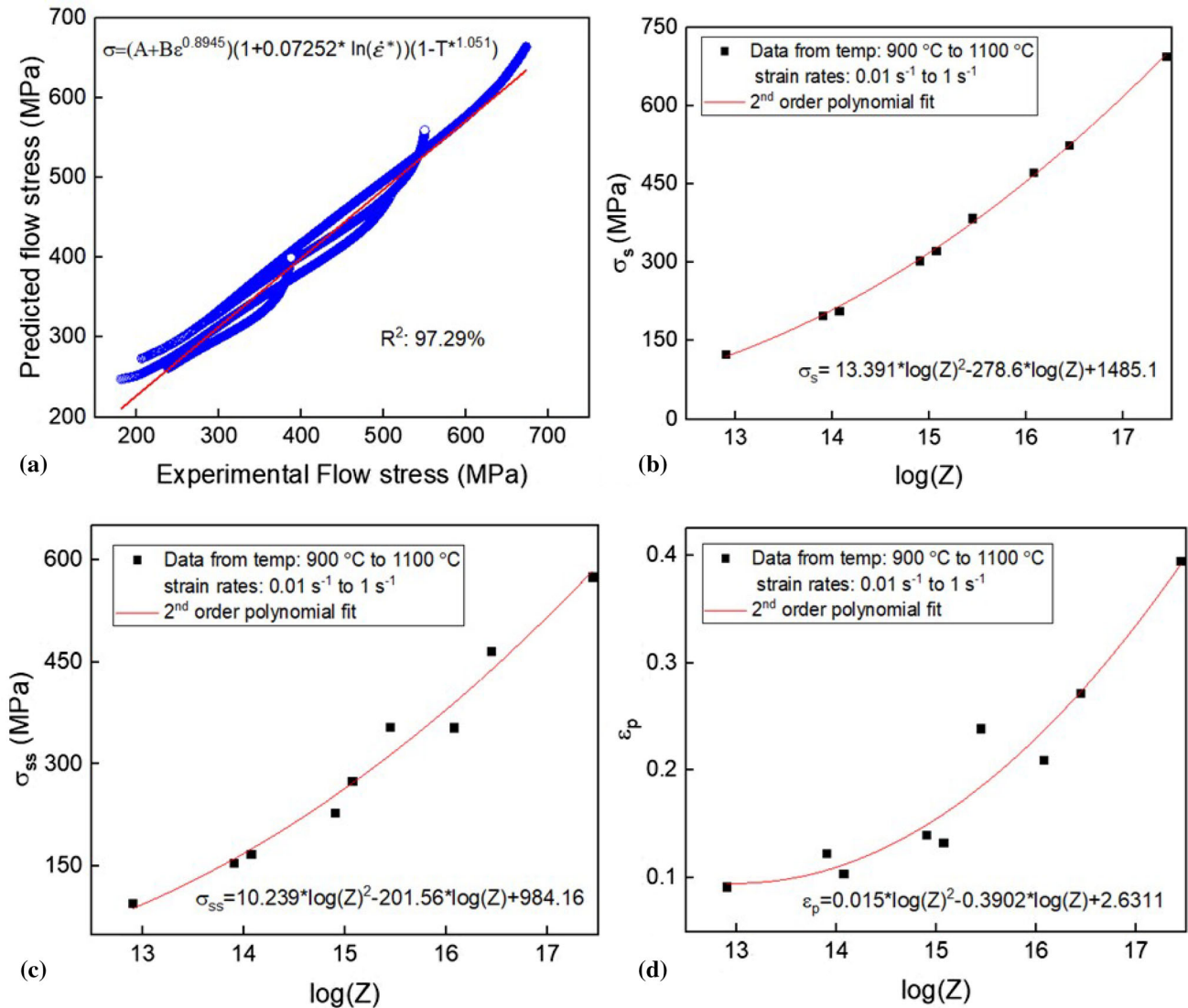


**Figure 8** a Comparison between the experimentally measured data with those predicted by the JC model for varying test conditions of the IN625 alloy over the work-hardening + dynamic

recovery (WH + DRV) region, and the relationship between  $\log(Z)$  with **b** saturation stress, **c** steady-state stress, and **d** the strain associated with the peak stress.

The accuracy and relevance of the JC + Avrami model for the prediction of flow behaviour during hot compression testing of IN625 alloy was evaluated using the experimentally measured data obtained at 950 °C, which was not used for the measurement of materials constant. The JC + Avrami model shows a relatively good convergence towards the experimentally measured data for both the work-hardening and flow softening stages (Fig. 9a, b). The model predictions are particularly more accurate for the tests carried out at low deformation temperatures and under higher strain rates. The deviation from the measured data under lower strain rates and at higher

temperatures can be mainly related to the materials constants where average values were considered for each case to reduce complexity. This in turn has resulted in less fidelity in identifying the relevant dominant deformation mechanisms at higher temperatures and under lower strain rates. Otherwise, the proposed JC + Avrami model can effectively be used for the estimation of flow stress in IN625 alloy at low temperatures (i.e., 900–1050 °C) and relatively high strain rates (i.e., 0.1–1 s<sup>-1</sup>) ranges.

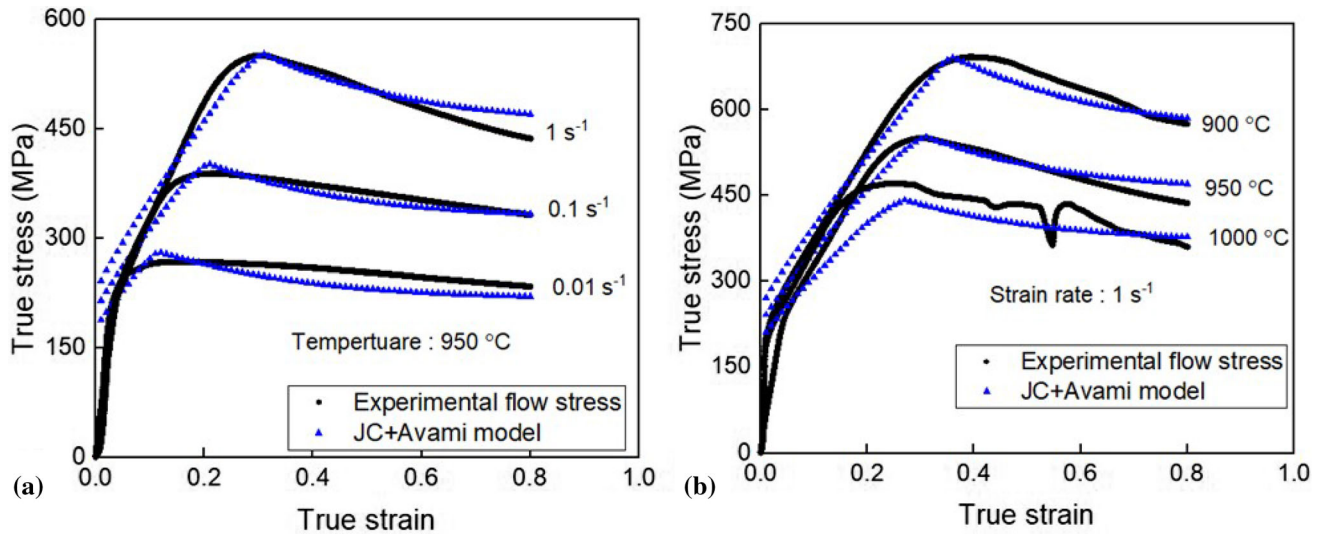


**Figure 9** Comparison between the results of combined JC + Avrami model prediction and the experimental results, **a** at 950 °C for varying strain rates, and **b** under 1 s<sup>-1</sup> strain rate at varying temperatures.

### FE simulation and industrial applicability

Constitutive equations describing material properties are the backbone of most FE simulations to accurately predict the deformation behaviour under industrial forging conditions. Reliable FE modelling benefits the industries to identify optimised forming conditions and to eliminate flow defects, whereby improving process efficiency. In the present study, the combined JC + Avrami material model was introduced in DEFORM®3D software as a user subroutine and used to simulate isothermal forging of a DTC sample

(Fig. 10a). The DTC geometry was opted to apply varying strain rates at a desired deformation temperature to simulate different strain and strain rate magnitudes usually experienced during industrial forging. The results of FE simulations conducted using DEFORM software suggest the likely strain and strain rate distributions throughout the DTC sample.

For the FE simulation, the DTC sample was considered as a deformable object and the top and bottom dies as rigid. The DTC was meshed with tetrahedral elements of 0.5 mm size on average. A uniform temperature of 900 °C was considered for

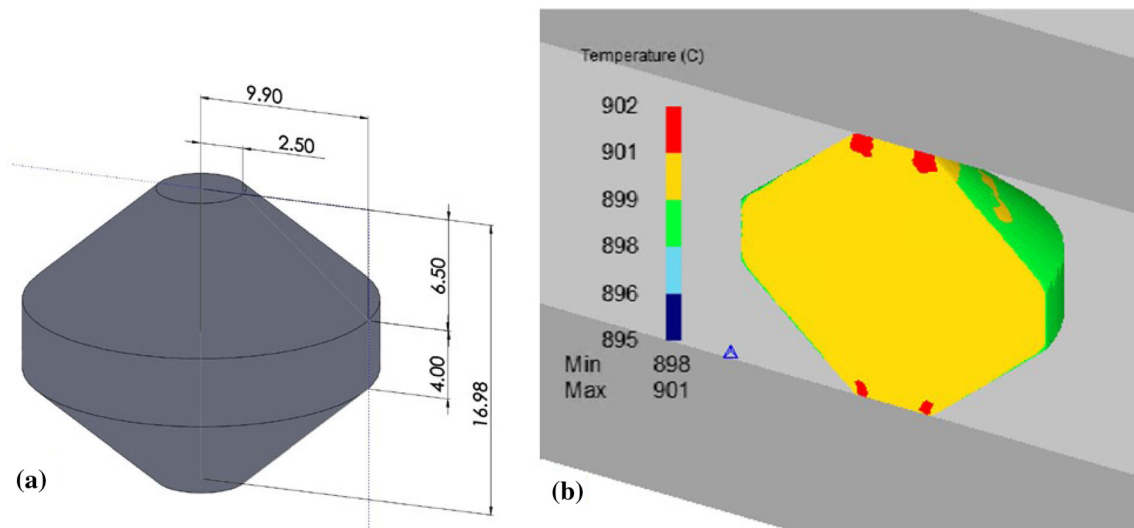


**Figure 10** **a** A 3D model of the double truncated cone (DTC) sample showing the dimensions in mm, and **b** DEFORM®3D simulation setup showing the temperature distribution of the sample at the beginning of the simulation at 900 °C.

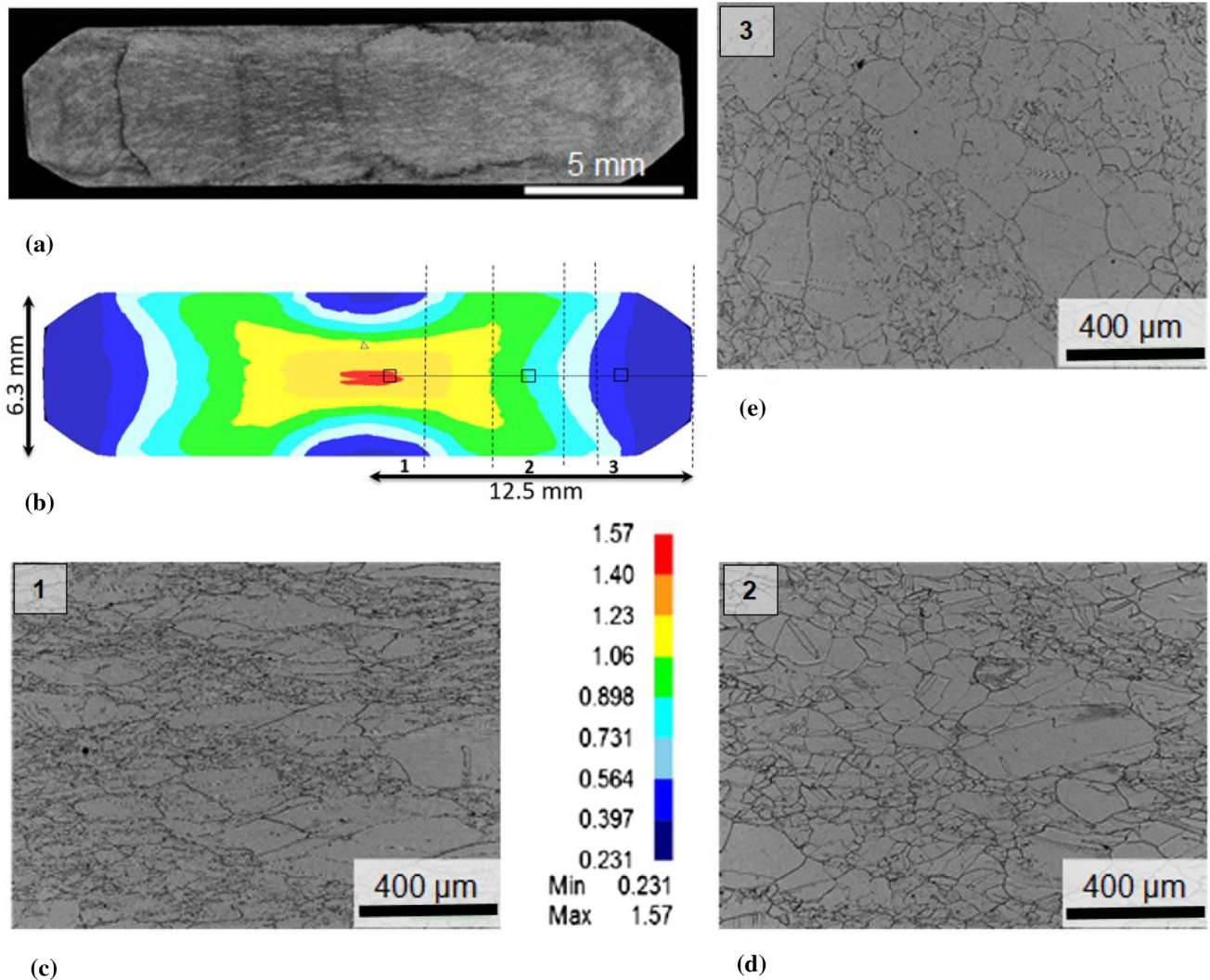


**Figure 11** a Montage of micrographs from optical microscopy from the cross-section of a DTC sample forged to 60% reduction, b the effective strain distribution predicted by FE simulation. c,

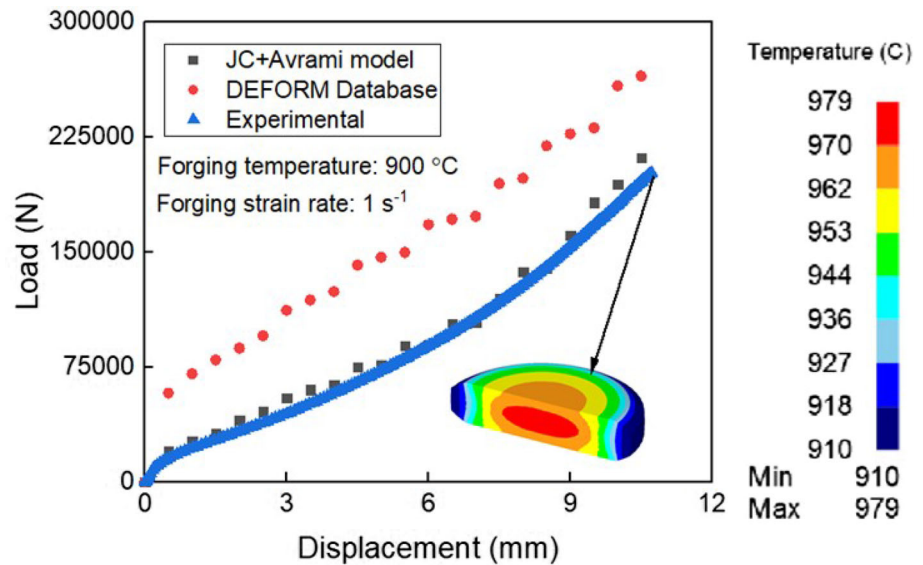
d and e optical micrographs of the areas with different strain magnitudes highlighted in b by 1, 2 and 3, respectively.

both DTC sample and the dies (Fig. 1 3b). The implementation of the combined JC + Avrami constitutive model was carried out at the test temperature of 900 °C and at strain rate of 1 s<sup>-1</sup>. This was to validate the suitability of the material model for the highest levels of stress imposed during isothermal forging. For the interaction between the sample and the dies, heat transfer and friction coefficients were considered as 2 N/mm/sec/C and 0.2, respectively, considering that the sample was coated with delta glaze and the dies were coated with boron nitride lubricants. The combined JC + Avrami material model was used as a substitute for material flow behaviour in the DEFORM®3D database, and all

other physical properties for IN625 alloy were considered from the DEFORM database.

The results of FE simulation were used to understand the magnitude and the distribution of effective strain as well as the temperature rise in the DTC sample with increase in the amount of strain imposed. In order to understand the deformation characteristics of the matrix in the forged DTC, optical microscopy was used. The macrostructure from the mid section of the forged billet showed the difference in the flow behaviour of grains under the influence of strain imposed during forging (Fig. 11a). Macrostructure revealed that equi-axed grains have changed to elongated grains in the direction perpendicular to loading direction at the centre of the

**Figure 12** Comparison between the results of FE simulations and the experimentally measured loads during isothermal compression testing of a DTC sample at 900 °C and under 1 s<sup>-1</sup> strain rate. The predicted temperature distribution of the deformed DTC sample showing deformation induced temperature raise of up to 979 °C is also provided.



forged billet. Also the grain boundaries of the elongated grains are decorated by fine equi-axed grains nucleated during the deformation. But the grains present in the areas close to edges of DTC were remained undeformed even after 60% reduction. This could be primarily due to difference in strain imposed. The predicted strain distribution by the FE simulation showed a variation in strain from the centre to the edges of the DTC sample (Fig. 11a). The amount of strain imposed is in the range of  $\sim 1.6$  to  $\sim 0.2$  after 60% reduction. Possibility of creating spectrum of strains using DTC sample is one of the major advantage against the classical cylindrical samples. Also adopting DTC sample geometry avoids the testing of many cylindrical samples to study the effect of parameters like strain rate, strain and temperature to understand the hot deformation behaviour of materials [24]. Higher magnification micrographs from the selected locations (marked as 1, 2 and 3 in Fig. 11b) clearly shows the presence of elongated grains with fine recrystallised grains along their grain boundaries, forming necklase structure, at the centre of the DTC (Fig. 11a) and coarse grains towards the edge of the sample. This can be linked to the strain magnitude changing from  $\sim 1.5$  in the core to  $\sim 0.2$  in the edge of the DTC sample.

Further, to evaluate the suitability of the combined JC + Avrami material model, the predicted load (FE simulated) was compared with the experimentally measured load during testing of the DTC sample (Fig. 12). A very good agreement was obtained

between the predicted load and the measured data. For the purpose of comparison with the JC + Avrami material model, an FE simulation was also conducted based on the existing database in DEFORM and the result is also presented in Fig. 12. The result of FE simulation based on the DEFORM database overestimates the required load for the deformation of the DTC sample significantly, compared to the JC + Avrami material model. However, the combined JC + Avrami material model can only be used for forging at temperatures below 1050 °C and under strain rates above 0.01 s<sup>-1</sup>, in its current form. This can be modified by using appropriate constants and coefficients in the relevant equations explained earlier, to predict different stages of the flow behaviour by being able to predict relevant microstructure evolutionary mechanisms such as work-hardening, dynamic recovery and recrystallisation, as opposed to averaged values.

## Conclusions

The deformation behavior of IN625 alloy, during isothermal hot compressions at a range of temperatures and strain rates were investigated. An innovative constitutive material model was proposed by combining Johnson–Cook and Avrami approaches, based on the results of compression tests. The main findings of this study are concluded as the following:

- The material exhibited significant work-hardening at low temperatures and under high strain



rates, followed by flow softening where the material microstructure undergoes dynamic recrystallisation.

- Discontinuous dynamic recrystallization (DDRX) was seen to be the principal recrystallisation mechanism at lower temperatures which lead to the formation of necklace structure (i.e., fine grains around the parent grain).
- The increase in dynamic recrystallisation at higher temperatures suggests that more microstructural mechanisms such as dynamic recovery, recrystallisation and growth become active, contributing to microstructure evolution.
- The dissolution of carbide at temperatures beyond solvus temperature enhances the grain growth.
- The combined JC + Avrami material model was successfully incorporated into DEFORM®3D simulation tool as a user subroutine.
- A better prediction was achieved by the FE simulation using the combined JC + Avrami material compared to the existing material database.

out at the Advanced Forming Research Centre (AFRC), University of Strathclyde, which receives partial financial support from the UK’s High Value Manufacturing CATAPULT.

**Open Access** This article is licensed under a Creative Commons Attribution 4.0 International License, which permits use, sharing, adaptation, distribution and reproduction in any medium or format, as long as you give appropriate credit to the original author(s) and the source, provide a link to the Creative Commons licence, and indicate if changes were made. The images or other third party material in this article are included in the article’s Creative Commons licence, unless indicated otherwise in a credit line to the material. If material is not included in the article’s Creative Commons licence and your intended use is not permitted by statutory regulation or exceeds the permitted use, you will need to obtain permission directly from the copyright holder. To view a copy of this licence, visit <http://creativecommons.org/licenses/by/4.0/>.

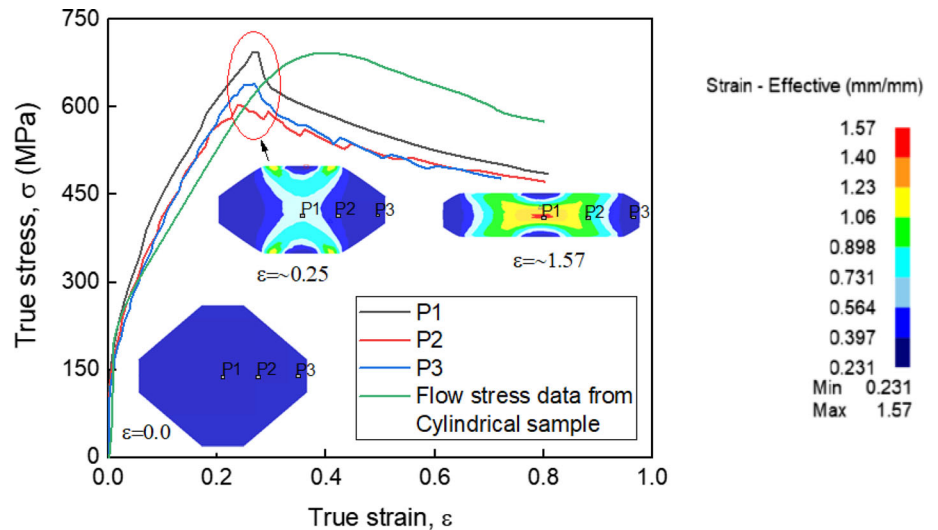
### Acknowledgements

The authors would like to acknowledge the financial support provided by Rolls Royce Plc for this project. The experimental and simulation works were carried

### Appendix 1

The true-stress versus true-strain curves were extracted from the results of FE simulation for the DTC geometry at three locations namely P1, P2 and P3, as highlighted in Fig. 13. P1, P2 and P3

**Figure 13** Comparison between the plots of true-stress versus true-strain curves extracted at three locations, namely P1, P2 and P3, from the results of FE simulation of the DTC sample, and the experimentally measured flow curve for the IN625 material tested at 900 °C under 1 s<sup>-1</sup> strain rate.





correspond to areas in the DTC which are simulated to be experiencing varying strain rates during forging. These are plotted against the most closer experimentally measured condition which was the test conducted at 900 °C under 1 s<sup>-1</sup> strain rate (Fig. 13), up to ~ 0.8 strain. The plot show a relatively good match overall, although the peak stress appear to be reached at lower strains in the results of simulation. This is not significant as firstly the condition for the deformation in DTC is not exactly the same as a standard compression test, and secondly there is variation in strain rate of the nodal points selected within the result of FE simulation.

## References

- [1] Zhang Y-C, Jiang W, Tu S-T, Zhang X-C, Ye Y-J, Wang R-Z (2018) Experimental investigation and numerical prediction on creep crack growth behavior of the solution treated Inconel 625 superalloy. *Eng Fract Mech* 199:327–342
- [2] Cinoglu IS, Charbal A, Vermaak N (2020) Towards exploiting inelastic design for Inconel 625 under short-term cyclic loading at 600 °C. *Mech Mater* 140:103219
- [3] Karmuhilan M, Kumanan S (2021) A review on additive manufacturing processes of inconel 625. *J Mater Eng Perform* 31(4):2583–2592
- [4] Kou H, Li W, Ma J, Shao J, Tao Y, Zhang X, Geng P, Deng Y, Li Y, Zhang X, Peng F (2018) Theoretical prediction of the temperature-dependent yield strength of solid solution strengthening Nickel-based alloys. *Int J Mech Sci* 140:83–92
- [5] Jia Z, Gao Z, Ji J (2020) A mechanism for the evolution of hot compression cracking in inconel 625 alloy ingot with respect to grain growth. *Adv Eng Mater* 22(6):1901445
- [6] Benghalia G, Rahimi S, Wood J, Coules H, Paddea S (2018) Multiscale measurements of residual stress in a low-alloy carbon steel weld clad with IN625 superalloy. *Mater Perform Charact* 7:606–629
- [7] Mataveli Suave L, Cormier J, Bertheau D, Villechaise P, Soula A, Hervier Z, Hamon F (2016) High temperature low cycle fatigue properties of alloy 625. *Mater Sci Eng A* 650:161–170
- [8] Wang M, Zeng S, Zhang H, Zhu M, Lei C, Li B (2020) Corrosion behaviors of 316 stainless steel and Inconel 625 alloy in chloride molten salts for solar energy storage. *High Temp Mater Process (London)* 39(1):340–350
- [9] Mohammadi Zahrani E, Alfantazi AM (2012) Molten salt induced corrosion of Inconel 625 superalloy in PbSO<sub>4</sub>-Pb<sub>3</sub>O<sub>4</sub>-PbCl<sub>2</sub>-Fe<sub>2</sub>O<sub>3</sub>-ZnO environment. *Corros Sci* 65:340–359
- [10] Shahwaz M, Nath P, Sen I (2022) A critical review on the microstructure and mechanical properties correlation of additively manufactured nickel-based superalloys. *J Alloys Comps* 907:164530
- [11] Smith TM, Gabb TP, Kantzos CA, Thompson AC, Sudbrack CK, West B, Ellis DL, Bowman CL (2021) The effect of composition on microstructure and properties for additively manufactured superalloy 718. *J Alloys Comps* 873:159789
- [12] Mahalle G, Kotkunde N, Shah R, Gupta AK, Singh SK (2018) Analysis of flow stress behaviour of Inconel alloys at elevated temperatures using constitutive model. *J Phys Conf Ser* 1063
- [13] Guo QM, Li DF, Guo SL (2012) Microstructural models of dynamic recrystallization in hot-deformed Inconel 625 superalloy. *Mater Manuf Process* 27(9):990–995
- [14] Souza PM, Beladi H, Singh RP, Hodgson PD, Rolfe B (2018) An analysis on the constitutive models for forging of Ti6Al4V alloy considering the softening behavior. *J Mater Eng Perform* 27(7):3545–3558
- [15] Johnson GR (1983) A constitutive model and data for metals subjected to large strains, high strain rates, and high temperatures. In: *Proceedings 7th international symposium on ballistics*, The Hague, pp 541–547
- [16] Jia Z, Sun X, Ji J, Wang Y, Wei B, Yu L (2021) Hot deformation behavior and dynamic recrystallization nucleation mechanisms of Inconel 625 during hot compressive deformation. *Adv Eng Mater* 23(3):2001048
- [17] Tehovnik F, Burja J, Podgornik B (2015) Microstructural evolution of Inconel 625 during hot rolling. *Mater Tehnol* 49(5):801–806
- [18] Li D, Guo Q, Guo S, Peng H, Wu Z (2011) The microstructure evolution and nucleation mechanisms of dynamic recrystallization in hot-deformed Inconel 625 superalloy. *Mater Des* 32(2):696–705
- [19] Wen D-X, Lin YC, Li H-B, Chen X-M, Deng J, Li L-T (2014) Hot deformation behavior and processing map of a typical Ni-based superalloy. *Mater Sci Eng A* 591:183–192
- [20] Chen F, Li K, Tang B, Liu D, Zhong H, Li J (2021) Deformation behavior and microstructural evolution of Inconel 625 superalloy during the hot compression process. *Metals* 11(5):824
- [21] Jia Z, Gao Z, Ji J, Liu D, Guo T, Ding Y (2019) Evolution of twin boundaries and contribution to dynamic recrystallization and grain growth of Inconel 625. *Adv Eng Mater* 21(9):1900426
- [22] Malmelov A, Fisk M, Lundback A, Lindgren LE (2020) Mechanism based flow stress model for alloy 625 and alloy 718. *Materials (Basel)* 13(24):5620

- [23] López B, Urcola JJ (2013) Hot deformation characteristics of Inconel 625. *Mater Sci Technol* 12(8):673–678
- [24] Wen D-X, Lin YC, Chen J, Chen X-M, Zhang J-L, Liang Y-J, Li L-T (2015) Work-hardening behaviors of typical solution-treated and aged Ni-based superalloys during hot deformation. *J Alloys Compd* 618:372–379
- [25] Badrishi CA, Kotkunde N, Salunke O, Singh SK, Datta SP (2019) Experimental and numerical investigations of Johnson Cook constitutive model for hot flow stress prediction of Inconel 625 alloy. *ICCMS* 2019:36–40
- [26] Lin YC, Wen D-X, Huang Y-C, Chen X-M, Chen X-W (2015) A unified physically based constitutive model for describing strain hardening effect and dynamic recovery behavior of a Ni-based superalloy. *J Mater Res* 30(24):3784–3794
- [27] Lin YC, Wen D-X, Deng J, Liu G, Chen J (2014) Constitutive models for high-temperature flow behaviors of a Ni-based superalloy. *Mater Des* 59:115–123
- [28] Chen Z-J, Lin YC, He D-G, Lou Y-M, Chen M-S (2021) A unified dislocation density-based model for an aged polycrystalline Ni-based superalloy considering the coupled effects of complicate deformation mechanisms and initial  $\delta$  phase. *Mater Sci Eng A* 827:142062
- [29] Lin YC, Wen D-X, Chen M-S, Chen X-M (2016) A novel unified dislocation density-based model for hot deformation behavior of a nickel-based superalloy under dynamic recrystallization conditions. *Appl Phys A* 122(9):1–16
- [30] Souza PM, Sivaswamy G, Hall L, Rahimi S (2022) An analysis of the forgeability of Ti–10V–2Fe–3Al  $\beta$  Titanium alloy using a combined estrin mecking and avrami material constitutive model. *Int J Mech Sci* 216:106975
- [31] Souza PM, Beladi H, Singh R, Rolfe B, Hodgson PD (2015) Constitutive analysis of hot deformation behavior of a Ti6Al4V alloy using physical based model. *Mater Sci Eng A* 648:265–273
- [32] Souza PM, Mendiguren J, Chao Q, Beladi H, Hodgson PD, Rolfe B (2019) A microstructural based constitutive approach for simulating hot deformation of Ti6Al4V alloy in the  $\alpha + \beta$  phase region. *Mater Sci Eng A* 748:30–37
- [33] Godasu AK, Prakash U, Mula S (2020) Flow stress characteristics and microstructural evolution of cast superalloy 625 during hot deformation. *J Alloys Compd* 844:156200
- [34] Lin YC, Chen M-S, Zhong J (2008) Prediction of 42CrMo steel flow stress at high temperature and strain rate. *Mech Res Commun* 35(3):142–150
- [35] Semiatin SL, Seetharaman V, Weiss I (1999) Flow behavior and globularization kinetics during hot working of Ti–6Al–4V with a colony alpha microstructure. *Mater Sci Eng A* 263(2):257–271
- [36] Luo J, Li M, Yu W, Li H (2010) The variation of strain rate sensitivity exponent and strain hardening exponent in isothermal compression of Ti–6Al–4V alloy. *Mater Des* 31(2):741–748
- [37] Stüwe HP, Les P (1998) Strain rate sensitivity of flow stress at large strains. *Acta Mater* 46(18):6375–6380
- [38] Zener C, Hollomon J (1944) Effect of strain rate upon plastic flow of steel. *J Appl Phys* 15(1):22–32
- [39] Sims CJJW (1972) Sons, WC Hagel the superalloys, pp 3–29
- [40] Singh JB (2022) Alloy 625: microstructure, properties and performance. Springer
- [41] Belyakov A, Dudova N, Tikhonova M, Sakai T, Tsuzaki K, Kaibyshev R (2012) Dynamic recrystallization mechanisms operating under different processing conditions. *Mater Sci Forum* 706–709:2704–2709
- [42] Souza PM, Hodgson PD, Rolfe B, Singh RP, Beladi H (2019) Effect of initial microstructure and beta phase evolution on dynamic recrystallization behaviour of Ti6Al4V alloy—an EBSD based investigation. *J Alloys Compd* 793:467–479
- [43] Puchi-Cabrera ES, Staia MH, Guérin JD, Lesage J, Dubar M, Chicot D (2014) An experimental analysis and modeling of the work-softening transient due to dynamic recrystallization. *Int J Plast* 54:113–131
- [44] Huang K, Logé RE (2016) A review of dynamic recrystallization phenomena in metallic materials. *Mater Des* 111:548–574
- [45] Chao Q, Hodgson P, Beladi H (2014) Ultrafine grain formation in a Ti–6Al–4V alloy by thermomechanical processing of a martensitic microstructure. *Metall Mat Trans A* 45:1–13
- [46] Ponge D, Gottstein G (1998) Necklace formation during dynamic recrystallization: mechanisms and impact on flow behavior. *Acta Mater* 46(1):69–80
- [47] Gholinia A, Humphreys FJ, Prangnell PB (2002) Production of ultra-fine grain microstructures in Al–Mg alloys by conventional rolling. *Acta Mater* 50(18):4461–4476
- [48] He G, Liu F, Huang L, Huang Z, Jiang L (2016) Microstructure evolutions and nucleation mechanisms of dynamic recrystallization of a powder metallurgy Ni-based superalloy during hot compression. *Mater Sci Eng A* 677:496–504
- [49] Johnson G, Cook W (1983) A constitutive model and data for metals subjected to large strains, high strain rates and high temperatures
- [50] He A, Xie G, Zhang H, Wang X (2013) A comparative study on Johnson-Cook, modified Johnson-Cook and Arrhenius-type constitutive models to predict the high temperature flow

stress in 20CrMo alloy steel. Mater Des 1980–2015(52):677–685

[51] Nash P (1991) Ni–Cr system, phase diagrams of binary nickel alloys. ASM International, Materials Park, pp 75–84

**Publisher's Note** Springer Nature remains neutral with regard to jurisdictional claims in published maps and institutional affiliations.

Springer Nature or its licensor (e.g. a society or other partner) holds exclusive rights to this article under a publishing agreement with the author(s) or other rightsholder(s); author self-archiving of the accepted manuscript version of this article is solely governed by the terms of such publishing agreement and applicable law.